Precision Engineering 100 (2026) 593–602

Contents lists available at ScienceDirect

Precision Engineering

journal homepage: www.elsevier.com/locate/precision

Study of the influence of cutting speed on diamond turning machining mechanisms for NiP

L. Yang [a], J. Redford [b], T. Liu [c], B. Dutterer [a], G. Caskey [a], N. Li [c], C. Evans [a,b,*], Y. Chen [a,**]

[a] University of North Carolina at Charlotte, US
[b] National Institute of Standards and Technology, US
[c] Los Alamos National Laboratory, US

A B S T R A C T

Diamond turning of nickel-phosphorous (NiP) has been widely researched. Although the tool geometry and cutting parameters have been investigated previously, the fundamental material removal mechanisms from a material perspective are still in demand to assist material designs for precision parts in harsher environments. Fundamentally, the material removal mechanism and associated phase transformations are governed by the severe plastic deformation and high strain rates induced at the tool tip. To investigate the role of strain rate, this study employs a simplified experimental design: we strictly maintain constant tool geometry, feed rate, and depth of cut, while systematically varying only the cutting speed (m/s) with a combination of cutting radius and spindle speed to indicate the influence of strain rate. This is achieved through a comparison of surface topography, chip structure, near-surface microstructure, and composition profile. The cutting speed varies by a factor of 50. Our results show that the increase in cutting speed induces higher surface roughness (*Sq*, root mean square roughness) and higher slope of the profile (*Sdq*, root mean square slope). The roughness shape bias (*Ssk*, skewness) is independent of cutting speed but is inversely related to the diameter of the cutting location on the sample disc. Phase transformation, more specifically, crystallization of amorphous NiP is commonly seen in chips for all cutting speeds. However, near-surface microstructural analysis shows that at the low cutting speed, there is no crystallization at the surface. The increase in cutting speed results in the crystallization of amorphous NiP and a P-depleted layer of 15.9 nm at the surface. The measured thickness of the depleted layer by energy-dispersive X-ray spectroscopy (EDS) is close to that of the crystallized layer of 14.2 nm. This study indicates that to achieve high surface quality, the cutting speed should be below a threshold value that induces crystallization in chips and near-surface damage of amorphous NiP.

1. Introduction

Nickel-phosphorous (NiP) coatings with unique properties of high hardness, wear resistance, and corrosion protection make them valuable for various industrial applications, such as digital printing parts, injection mold dies, and aspheric/freeform mirrors [1]. There are two types of NiP coatings that are widely used: electroless and electroplated NiP. The widely used electroless NiP coatings with uniform thickness are produced through a chemical reduction process, which is especially advantageous for coating complex geometries, which allows further manufacturing for different purposes. For example, back in 1980, Johnson demonstrated that the ultra-black electroless NiP can be successfully tuned by surface morphology modification by chemical etching [2]. On the other hand, electroplated NiP coatings can achieve thicker layers and higher phosphorus (P) content [3], enhancing durability and corrosion resistance for demanding applications in harsh environments. However, electroplated NiP is not as widely available as electroless NiP [4]. It is notable that research on NiP with new microstructure, such as incorporating different types of particles [5,6] is ongoing, aiming for better properties.

In general, NiP deposits are classified into three categories: low (1 wt % to 5 wt %), medium (5 wt % to 8 wt %), and high (9 wt % and above) P deposits. The common trend is that low-P NiP has a crystalline structure, and with the increase in P, the structure becomes a mixture of amorphous and crystalline phases or even fully amorphous [7]. The electroplating method has been used for very high P NiP. P content can reach up to 25 atomic % P in the crystalline form (pure compound, Ni_3P) and up to about 19 atomic % P in amorphous samples (eutectic composition of Ni and Ni_3P) [4,8]. The different structures of NiP play a critical role [4] in determining the surface quality of machined final products (i.e., optics and other precision parts) by ultra-precision manufacturing processes.

Ultra-precision manufacturing processes employing single-crystal diamond cutting tools, variously referred to as single-point diamond turning (SPDT) or diamond milling, typically utilize multi-axis precision machines to achieve exceptional surface quality. Surface topography, as

* Corresponding author. University of North Carolina at Charlotte, US.
** Corresponding author.
E-mail addresses: cevans52@charlotte.edu (C. Evans), ychen103@charlotte.edu (Y. Chen).

https://doi.org/10.1016/j.precisioneng.2026.03.026
Received 27 November 2025; Received in revised form 18 February 2026; Accepted 22 March 2026
Available online 23 March 2026

well as tool and sub-surface signatures, depend on a complex array of process and tool parameters and inherent wear mechanisms. Historically, prior to the emergence of precision machining for optical quality surfaces, diamond tools were primarily utilized in the engraving of gratings and scale ruling, as well as for machining hard materials. It is notable that historical literature often used the phrase “diamond tool” ambiguously to describe either the specific geometry of the tool or the material used as the cutting edge [9].

Conceptually, these processes are relatively simple [10]; however, as noted by Patterson, “beauty is in the details” [11]. Consistently reproducing parts with nanometer-scale tolerances and specific surface topographies requires mastery over several intertwined variables, including undisclosed plating processes, complex machining parameter sets, and varying material behavior.

First, a primary source of this complexity is the tool itself. Drawing on their origins as ruling tools, early crystalline diamond tools were manufactured from “near gem quality” natural diamonds. As a class, these natural stones can possess a wide variety of chemical impurities and inclusions that significantly alter their mechanical, thermal, electrical, and optical properties [12]. Diamond tools vary in different machining processes: variations in crystal orientation, edge sharpness, and the presence of micro-defects at the tool tip can significantly influence the final surface finish and tool longevity.

Second, wear/machining mechanisms are highly material-dependent. For example, different NiP forms have different interactions with the diamond tool, which determines diamond tool wear [13] and the sample surface morphology: tuning NiP structure by heat treatment and deposition parameters enabled Taylor et al. to reach diamond turned surface roughness less than 1 nm [14]. For NiP composed of a mixture of pure nickel (crystalline) and the compound Ni_3P (crystalline), an increase in P leads to a higher fraction of harder second-phase Ni_3P, which causes more abrasive wear in diamond tools [15]. For NiP with amorphous phase, lower tool wear is expected [3,4,16,17]. It is interesting to notice that in fully amorphous NiP, two types of amorphous phases with different stability have been discovered and the higher P content favors the more stable amorphous phase with lower tool wear [16,18,19], which is interpreted by the theory of chemical wear related unpaired d-shell electrons by Paul et al. [4]. The proposed interaction between unpaired d-shell electrons from the workpiece and diamond tool to form carbon-metal complexes fits the experimental data of different materials well.

Third, tool geometry and cutting parameters are fundamentally linked to variations in surface quality [20,21]. While material properties differ, achieving superior surface quality universally requires an optimized combination of feed rate, spindle speed, depth of cut, and tool geometry. For instance, Geng et al. [22] and Xiong and Wu [23] demonstrated that minimizing feed rates is critical for improving surface quality in ZnSe and Ti6Al4V alloys, respectively. Zhang et al. [24] demonstrate that the depth of cut has the greatest impact on A100 steel and 300M steel, and the spindle speed has the smallest. Kim et al. [25] highlighted spindle speed as the most influential factor for aluminum, a trend supported by Cheung and Lee [15], who observed that higher speeds combined with larger tool nose radii yield smoother finishes. Similarly, Bao et al. [26] found that for NiP, optimal surface quality is achieved through a comparable balance of high spindle speed, low feed rate, and specific tool geometry. Collectively, these studies emphasize that while material properties differ, achieving superior surface quality universally requires a tailored combination of minimized feeds and optimized cutting speeds. The material removal mechanisms are not the focus of these studies.

Benefiting from the advances in electron microscopy characterization techniques, especially transmission electron microscopy (TEM), fundamental materials information during the machining process have been successfully adopted to investigate the material removal mechanism in several ceramics at the nanometer scale: researchers can identify the formation mechanism of near-surface damage, in terms of competing mechanisms of amorphization, poly-crystallization, microcracking, and dislocation formation in plunge-cut silicon [27] and diamond turned GaAs ceramics [28]. Motivated by these studies, we aim to correlate surface morphology, near-surface damage and chip structure at the nanometer scale for the first time. It is hypothesized that the phase transformation, more specifically crystallization, due to different machining conditions, may occur, and significantly affect surface morphology and near-surface damage. Fundamentally, the material removal mechanism and associated phase transformations are governed by the severe plastic deformation and high strain rates induced at the tool tip. While variations in tool geometry and feed rates inevitably alter the effective cutting mechanics, they introduce complex geometric variables that can obscure the underlying kinetic effects. To decouple these factors, this study employs a simplified experimental design: we maintain constant tool geometry, feed rate, and depth of cut, while systematically varying only the cutting speed (m/s) with a combination of cutting radius and spindle speed. This approach allows us to directly modulate the strain rate, thereby isolating its specific role in driving microstructural evolution and surface formation.

2. Experiment

The NiP coatings (OptaKoat®) for diamond turning were electroplated by TechMetals Inc. on 6061-T6 Aluminum substrate with 70 mm in diameter. The thickness of the coating was 101.6 μm. This coating is highly reflective and specifically developed for the optics and diamond-turning industry. The diamond turning was performed on a [†]Moore Nanotechnology 650FGv2. This is a facing operation on one end of the cylindrical test piece. The diamond cutting tool tip has a 0.5 mm nominal nose radius. The rake angle is 0^o and the clearance angle is 12.5^o. The feed rate/crossfeed is 10 μm/rev. The depth of cut (DoC) is 2.5 μm. A range of cutting speeds (m/s) is accomplished by a combination of spindle speeds (200 rpm to 2000 rpm) and turning diameters (11 mm to 65 mm) (Fig. 1). Variation in cutting speed by approximately a factor of 50 is achieved from 0.12 m/s to 6.81 m/s. Prior to the formal cutting, a pre-machining (diamond turning) was performed over the entire surface at 200 rpm and a feed/rev of 5 μm, ensuring that the cutting speed (surface speed) in pre-machining is less than the experimental conditions.

Surface topography analysis by a series of partially overlapping areal scans of each sample was acquired using [†]Zygo NexView Coherence Scanning Interferometer (CSI) with a 50 × mirau objective located at the University of North Carolina at Charlotte. The individual scans were stitched together using the instrument's native Mx™ software to increase the nominal field of view (FOV) without changing the spatial sampling or optical resolution of 0.17 μm and 0.52 μm, respectively. The stitched height maps of each sample were cropped to a consistent planar area of approximately 500 μm × 1000 μm, parallel and perpendicular to the dominant lay direction for subsequent analysis and surface parameter evaluation. Surface parameter statistics were also computed for 45 individual 170 μm × 170 μm scans for each surface condition. In both cases (stitched and individual scans), a 6th-order polynomial fit was used to level and remove any low-frequency form deviations in the surface topography data before parameter evaluation; no high- or low-pass filtering was utilized.

X-Ray diffraction experiments (XRD) were performed on [†]Rigaku

[†] NIST DISCLAIMER:

Certain commercial equipment, instruments, or materials are identified in this paper to specify the experimental procedure adequately. Such identification is not intended to imply recommendation or endorsement by NIST, nor is it intended to imply that the materials or equipment identified are necessarily the best available for the purpose. This material is declared a work of the U.S. Government and is not subject to copyright protection in the United States. Approved for public release; distribution is unlimited.

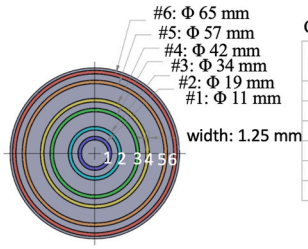

Cutting speed = (diameter · π) · rpm

Sample #	Diameter (mm)	Spindle (rpm)	Cutting speed (m/s)
1	11	200	0.12
2	19	2000	1.99
3	34	200	0.36
4	42	2000	4.40
5	57	200	0.60
6	65	2000	6.81

Fig. 1. The locations for machining on the component surface (unit: mm). Six cutting speeds are designed by combining different spindle rpm and diameters.

SmartLab® at room temperature. Bragg-Brentano XRD and Grazing Incidence (GI)-XRD induced by 1^{o}, 5^{o}, and 9^{o} incidence angles were used to examine the phase of the surface layer. Transmission Electron Microscopy (TEM) foils were prepared by Focus Ion beam (FIB) (model: †ThermoFisher Quanta 3D FEG). TEM and energy-dispersive X-ray spectroscopy (EDS) were carried out in a †JEOL 2100 transmission electron microscope operated at 200 keV at the University of North Carolina at Charlotte and a †Titan G2 80-200 Scanning TEM (STEM) at Los Alamos National Laboratory.

3. Results and discussion

This section presents a comprehensive analysis of the surface integrity of diamond-turned electroplated NiP. First, the surface topography is evaluated using statistical roughness parameters (*Sq*, *Ssk* and *Sdq*) and Power Spectral Density (PSD) to quantify the degradation of surface quality at higher cutting speeds. Subsequently, the underlying material removal mechanisms are elucidated through microstructural characterization of chips and the near-surface layer using XRD, TEM, and EDS. The combined results establish a correlation between the speed-induced increase in roughness and the onset of localized phase transformation (crystallization) and elemental segregation.

3.1. Surface topography analysis

This subsection details the evolution of surface topography across varying cutting speeds (0.12 m/s to 6.81 m/s). The topography of all six rings manufactured with different cutting speeds is shown in Fig. 2. As designed, the dominant spatial period between peaks or troughs is approximately 10 μm for all cutting speeds (see Fig. 2c). Small variations in this fundamental period are primarily caused by subtle differences in the effective feed per revolution, resulting in variations in the uncut chip thickness. Although the fundamental period appears consistent between samples, the shape of the imparted surface profile varies, as shown in the overlapped cutting-speed-dependent surface profiles in Fig. 2c. The difference in profile shape may be attributed to variations in cutting force and elastic spring-back. Qualitatively, lower cutting speed induces lower surface roughness (peak-to-valley height difference). The calculated average ± one standard deviation of the maximum total height (distance between the highest peak and lowest valley) for the six measured primary profiles shown in Fig. 2c is 31.5 nm ± 3.4 nm, comparable to the theoretical estimate of 25 nm, calculated by $Pt \approx f_t^2/8R$ [29], where R is the nominal 0.5 mm nose radius of the diamond tool, and f_t is the 10 μm/rev programmed feed rate. Discrepancies between the theoretical calculation and measured values are expected as the formula assumes perfect geometry and kinematics. In practice, minor differences in the assumed edge radius and feed rate, in addition to edge wear, vibrations, and material-specific ductile-brittle transitions, affect the final surface profile.

Three key statistical parameters were selected from the ISO 25178-2 standard [30] to describe surface characteristics: *Sq* (Root Mean Square Roughness), *Ssk* (Skewness), and *Sdq* (Root Mean Square Slope). *Sq* is the standard deviation of the surface's height distribution and provides a quantitative and commonly used general measure of surface roughness magnitude. *Ssk* measures the asymmetry of the distribution of surface texture height values. Zero skewness indicates a symmetric height distribution of material about the mean plane of the surface, whereas a positive value suggests a surface with more prominent peaks. *Sdq* quantifies the root mean square (rms) slope of the textural features on a surface. Overall, measured *Sq* and *Sdq* increase with cutting speed. There is no clear trend for *Ssk*. A more quantitative correlation is as follows.

Columns three to five in Table 1 list calculated roughness values for the stitched 500 μm × 1000 μm areal height map in Fig. 2a (top number), containing approximately 21 individual height maps and the average and standard deviation of 45 individual 170 μm × 170 μm areal height maps (bottom number). See the top center image of Fig. 2a for size reference. Note that the surface roughness value(s) for the stitched height map were always within one standard deviation of the mean values obtained from the 45 individual height maps that consisted of much smaller evaluation areas. Fig. 3 includes box plots of the surface parameter data for the individual CSI measurements plotted against cutting speed (left) and nominal ring diameter (right). The interquartile range (IQR) of the data is shown as grey boxes; the lower and upper bounds of the whiskers are calculated as Q1 - 1.5 · IQR and Q3 + 1.5 · IQR, respectively. Values above or below this range are considered as outliers that are created when roughness parameters are computed on a measured area of the surface that contains small debris or defects (see dark spots in Fig. 2a, for example). The horizontal line (−) within the grey boxes represents the median of the data and the (×) represents the mean. The latter can be skewed in some cases (see *Ssk* plots in Fig. 3) due to the presence of a few extreme outliers in the data, some extending beyond the y-axis range of the plot(s). The outliers were omitted from the computation of the statistics presented in Table 1 and the Pearson correlation coefficients depicted in Fig. 3. However, they were retained in the bar plots in Fig. 3 to visualize their presence and illustrate their potential to introduce bias in the mean estimate if not properly controlled for. Upon removal of the outliers, the mean and median of the surface parameter data for each case exhibited strong concordance. The variation in *Sq* in Fig. 3 for a given cutting speed or nominal ring diameter is about 0.25 nm. A negative trend in the average *Sq* values is observed for cutting speeds ranging from 0.12 m/s to 0.6 m/s, while a positive trend is observed for cutting speeds ranging from 0.6 m/s to 6.81 m/s.

The Pearson correlation coefficient (ρ) is employed to quantitatively assess the linear relationship between cutting speed and surface roughness parameters *Sq*, *Ssk* and *Sdq*. It is acknowledged that this metric does not capture non-linear dependencies; a low coefficient could theoretically result from a strong but non-monotonic relationship. However, the near-unity coefficients observed for *Sq* ($\rho = 0.97$) and *Sdq* ($\rho = 0.93$) indicate that the relationship between cutting speed and the roughness amplitude/slope is predominantly linear within the tested process window. In contrast, the low coefficient for Skewness (*Ssk*, $\rho = -0.51$) signals a weak linear relationship with cutting speed; instead, the strong correlation with diameter ($\rho = -0.85$) indicates that geometric factors play the primary role.

Power Spectral Density (PSD) analysis is an essential technique for evaluating surface topography in diamond turning, providing a detailed breakdown of surface features by their spatial frequencies. Mathematically, the PSD of a surface is calculated as the average of the square of the Fourier transforms for each row (or column) of an areal measurement. The graph provides insights into the spatial content of a surface, whereby the x-axis covers the range of spatial wavelengths captured within the measurement area. This analytical approach identifies periodic tool marks and discerns subtle variations in the surface topography, which are critical for the high-precision requirements of optical components. As expected, the strongest and 1st peak of spatial frequency is 100 cycles/mm, which corresponds to 10 μm spatial wavelength

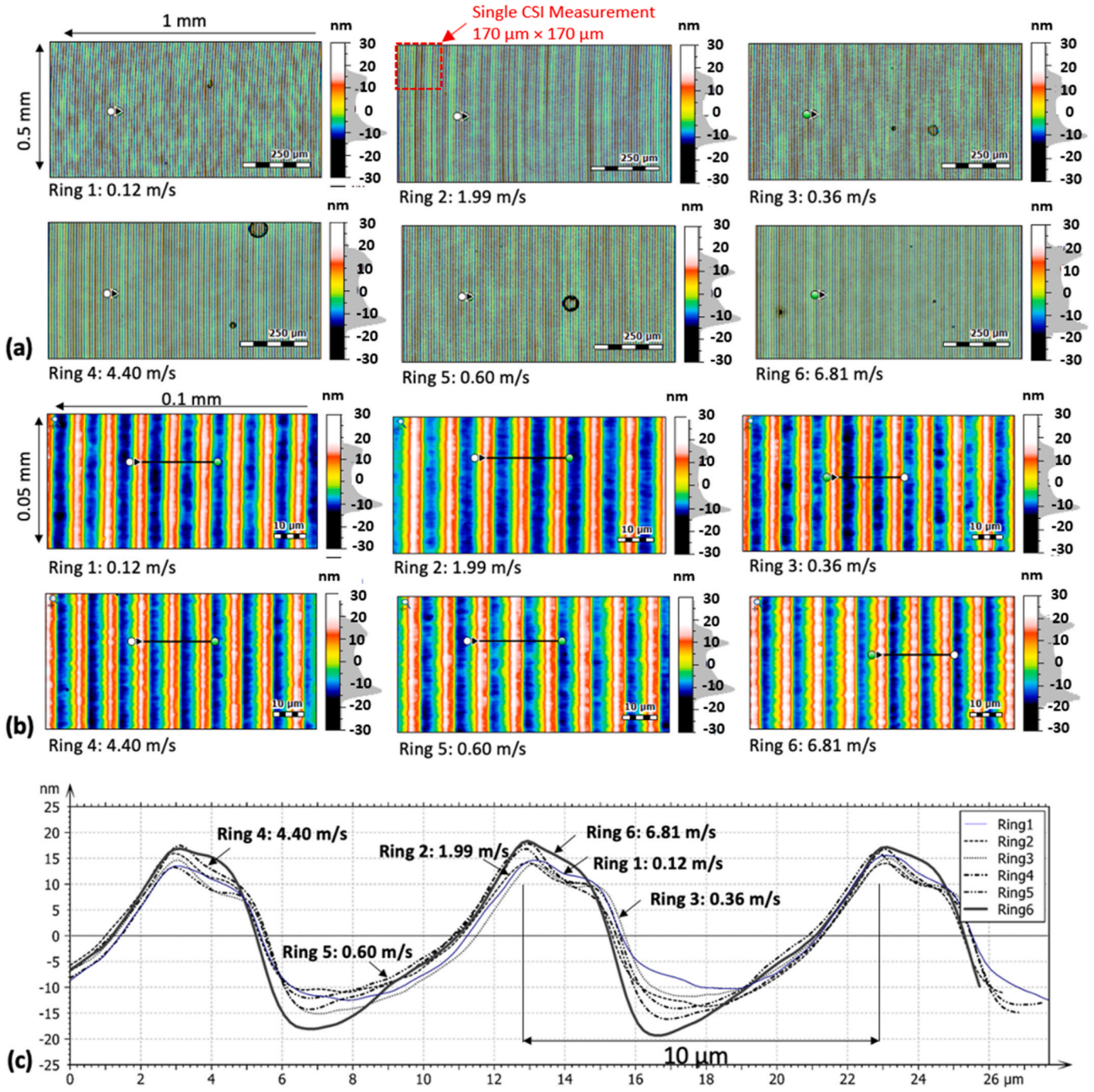

Fig. 2. (a) Cropped 0.5 mm × 1.0 mm areal topography CSI scans of turned surfaces. (b) Cropped 0.05 mm × 0.1 mm areal topography CSI scans of turned surfaces. (c) Localized profiles of the topography of machined surfaces at six different cutting speeds. The total height (*Pt*) measured for the primary profiles corresponding to rings 1 to 6 were 28.1 nm (ring 1), 28.3 nm (ring 2), 30.4 nm (ring 3), 33.7 nm (ring 4), 30.7 nm (ring 5), and 38.0 nm (ring 6).

Table 1
Statistical surface roughness calculated on 500 μm × 1000 μm stitched areal height map (top number) with average and standard deviation of 45 individual 170 μm × 170 μm height maps (bottom number) of turned surfaces. See Fig. 2a for reference.

Ring	Nominal Ring Dia (mm)	Cutting speed (m/s)	*Sq* (nm)	*Ssk*	*Sdq* (μm/mm)
#1	11	0.12	9.69	0.32	6.89
			9.73 ± 0.09	0.31 ± 0.01	6.99 ± 0.13
#2	19	1.99	10.00	0.36	7.34
			10.07 ± 0.14	0.35 ± 0.01	7.43 ± 0.12
#3	34	0.36	9.56	0.26	7.32
			9.58 ± 0.05	0.25 ± 0.02	7.46 ± 0.15
#4	42	4.40	10.74	0.21	8.21
			10.75 ± 0.11	0.21 ± 0.01	8.22 ± 0.10
#5	57	0.60	9.54	0.18	7.52
			9.52 ± 0.08	0.18 ± 0.02	7.58 ± 0.07
#6	65	6.81	12.12	0.16	9.24
			12.1 ± 0.07	0.15 ± 0.02	9.38 ± 0.16

(Fig. 4a). Each subsequent peak corresponds to an integer multiple of a fundamental frequency of 100/mm, forming a harmonic series due to the subtle irregularities that make up the approximate sinusoidal shape of the grooves. The magnified area on the 1st peak (Fig. 4b) shows that the peaks for Ring 1 to Ring 6 overlapped, indicating the consistency of turning marks in diamond turning of NiP.

3.2. Microstructure analysis of chips and near-surface damage

This subsection examines the sub-surface microstructural and chemical changes induced by the machining process. While continuous chips indicate a ductile cutting mode across all parameters, cross-sectional Transmission Electron Microscopy (TEM) and Energy Dispersive Spectroscopy (EDS) reveal a distinct material response limit. The aim is to provide a physical interpretation for the surface degradation observed in the topography analysis.

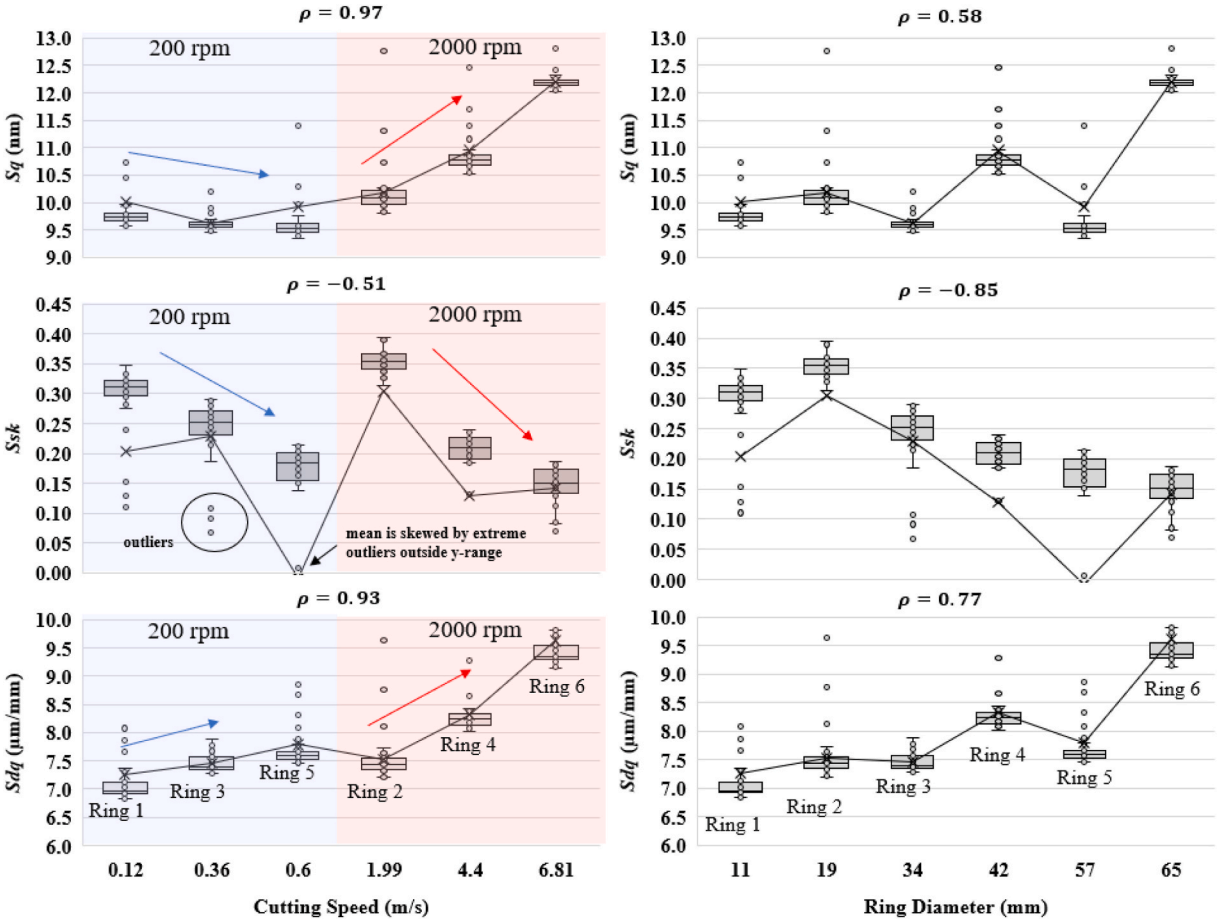

Fig. 3. *Sq*, *Ssk* and *Sdq* variations as a function of cutting speed (left) and ring diameter (right). Some extreme outliers in the data are out of the y-axis range and significantly skew the calculated mean values (e.g., mean *Ssk* value for ring 5). Pearson correlation coefficient (ρ) shown above each plot is computed after outlier removal. The interquartile range (IQR) of the data is shown as grey boxes; the lower and upper bounds of the whiskers are calculated as Q1 - 1.5 • IQR and Q3 + 1.5 • IQR, respectively. Values above or below this range are considered as outliers that are created when roughness parameters are computed on a measured area of the surface that contains small debris or defects.

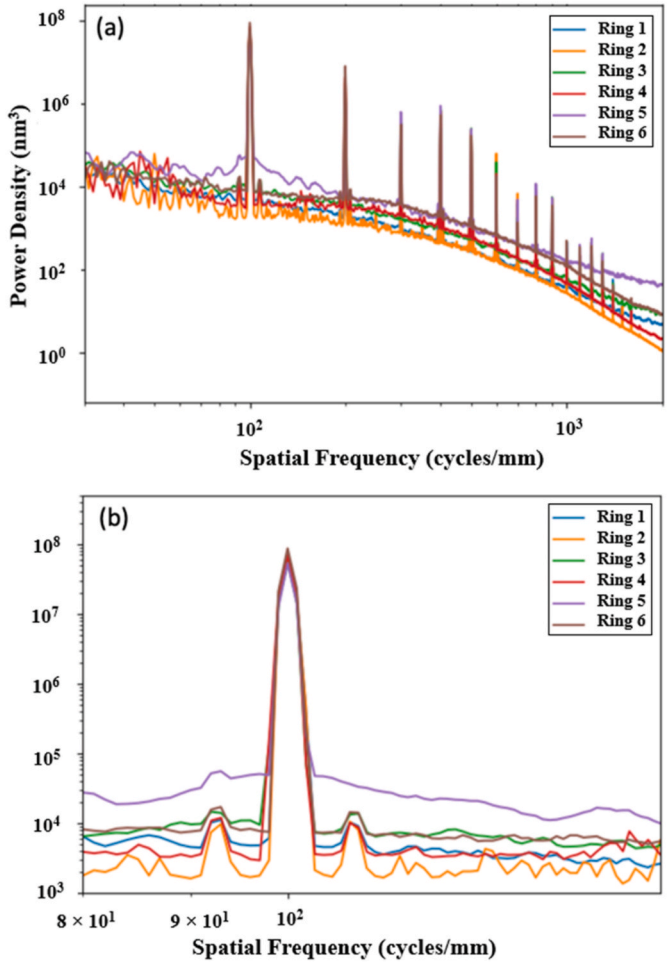

Fig. 4. (a) Power Spectral Density (PSD) of machined rings showing the effect of cutting speed on density spectrum. (b) PSD with limited range.

Bragg-Brentano XRD and grazing incidence XRD (GI-XRD) techniques were employed to characterize the crystalline phases of the surface material at different depths. The penetration depths during GI-XRD induced by 1°, 5°, and 9° incidence angles are 0.4 μm, 2.2 μm, and 4.1 μm, respectively. As shown in Fig. 5, no crystalline peaks are observed at different depths of layers, which suggests a fully amorphous or insignificant crystalline structure within the analyzed surface layer. XRD results also confirmed that the electroplated NiP has a fully amorphous structure before diamond turning.

For all six rings with different cutting speeds, the continuous chips indicate the ductile machining mode. Plastic deformation, in contrast to fracturing, dominates during the turning. TEM images and selected area diffraction (SAD) allow the examination of microstructure and phases at the nanometer scale. Long (continuous) chips (>2 mm) from Ring 1 (lowest cutting speed) and Ring 6 (highest cutting speed) were mounted to TEM grids. As the chip from diamond turning has various thicknesses, one side of the chip is electron transparent and was thoroughly examined by TEM. Two long chips (Ring 1 and Ring 6) are demonstrated in Figs. 6 and 7, respectively. It is noted that partial crystallization occurred during the chipping process for both samples, as a mixture of amorphous and crystalline phases was observed. Phase structure

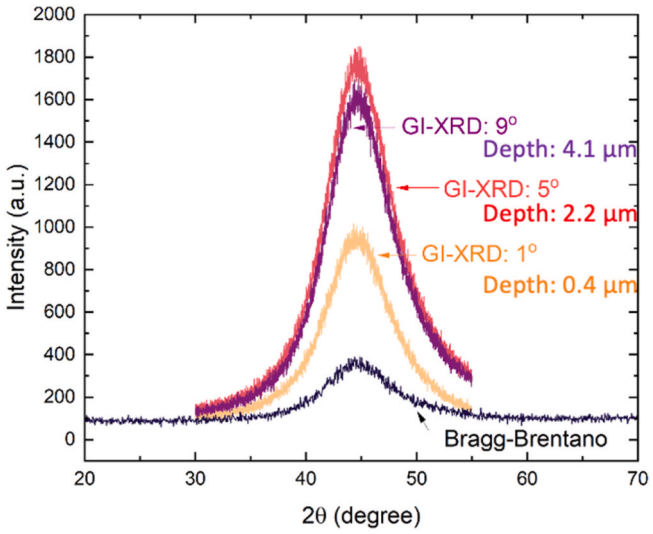

Fig. 5. Bragg-Brentano XRD and GI-XRD results showing the amorphous structure on the machined NiP surfaces.

overviews of the entire chips were collected, and the red lines were used to highlight the amorphous structure (no phase transformation) and the blue lines to represent the crystalline (phase transformation). The portion of crystallized regions is significant, accounting for 25% to 33% of the thinner edges of collected chips based on two long chips in this study. There is no obvious difference in shear banding behavior (the serration) for amorphous and crystallized regions.

Besides chips, the near-surface damage at different cutting speeds is compared. Cross-section TEM samples of the machined surfaces of Ring 1 (lowest cutting speed, Fig. 8) and Ring 6 (highest cutting speed, Fig. 9) were prepared by the FIB technique. The machined surfaces are protected by a Platinum (Pt) or carbon (C) layer. For Ring 1, no crystalized layer was detected on the surface (Fig. 8a). The inset SAD pattern shows a clear amorphous structure. High-resolution (HR)TEM micrograph (Fig. 8b) further confirms a clear interface between the Pt protective layer (nanocrystalline) and NiP layer (amorphous). On the other hand, for Ring 6, a layer of 14.2 nm ± 1.6 nm crystalized layer was observed (Fig. 9). The crystallized NiP layer contains nanocrystals of several nanometers in diameter, observed by HRTEM (Fig. 9c).

The element distribution of the machined surface is examined to study if the near-surface structure is correlated to elemental segregation/depletion. The surface composition profiles of Ring 1 (Fig. 10a–c) and Ring 6 (Fig. 10d–f) are collected by EDS line scan. Fig. 10b and e include Ni and P elements, as well as the elements of the protective layer, i.e., Pt and C, respectively. Fig. 10c and f include only Ni and P elements. We use Fig. 10b and e to define the surface location where the concentration of Ni and P is negligible (<1 %). Results in Figs. 10c and f shows P at the surface of Ring 1 is similar to the inside base materials of 18.2 atomic % ± 0.9 atomic % (10.5 % ± 0.5 % by weight), while in Ring 6, a P depleted layer with a thickness of 15.9 nm ± 0.3 nm and composition of 12.4 atomic % ± 0.6 atomic % (6.9 % ± 0.3 % by weight) is observed. The composition of base materials inside is 17.8 atomic % ± 3 atomic % (10.3 % ± 1.7 % by weight). The thickness of 15.9 nm is the lower limit of the P-depleted layer. As shown in Fig. 10f, the upper limit considers the surface as the interface defined above, and the lower limit only considers the length of the uniformly separated/depleted region. Statistical information of P elemental concentrations in

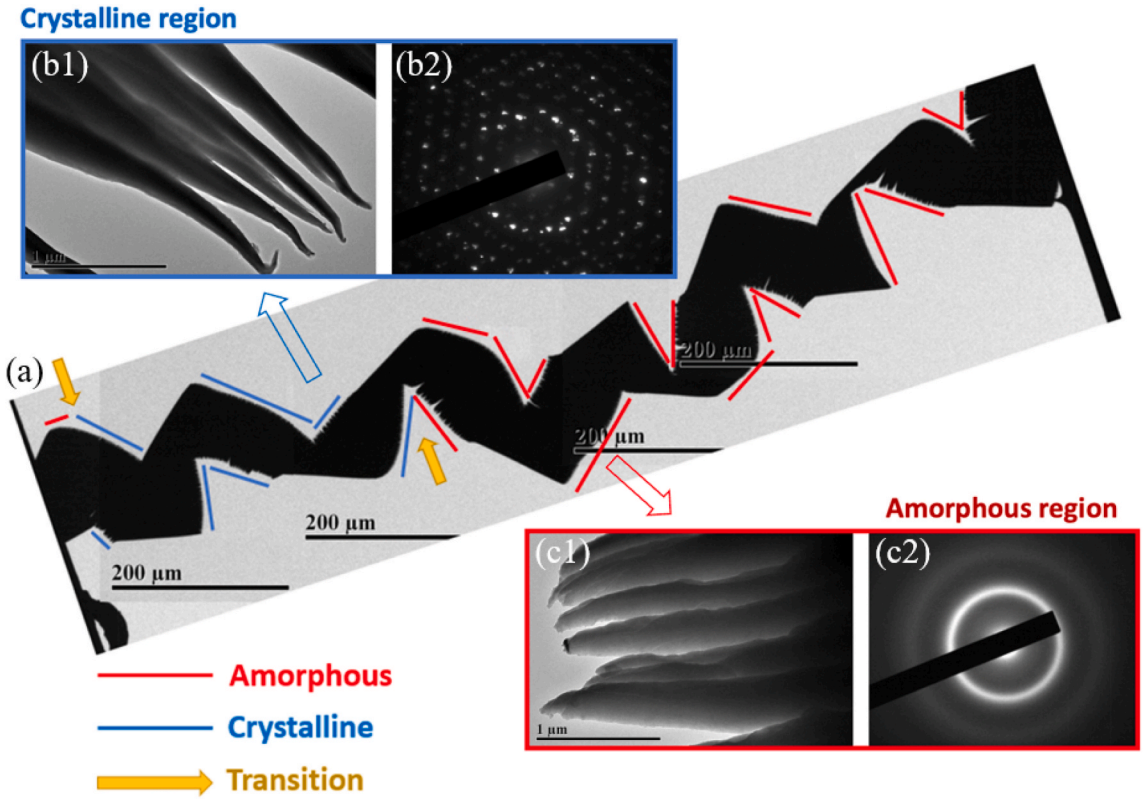

Fig. 6. TEM and SAD analysis showing a serration (shear banding) in the cutting chip from the lowest cutting speed (Ring 1). A mixture of amorphous structure and intermetallic is observed. (a) An overview of an entire chip with two ends bonded to a TEM grid. This is a TEM image stitched from multiple overlap low-magnification TEM images. The thinner edges of the entire chip have been examined thoroughly at higher magnification, which has two types of structure: crystalline and amorphous regions. The labeled red lines on the chip represent the regions that are amorphous, while the blue line represents crystalline regions. One representative crystalline region (b1) and amorphous region (c1) are shown. The contrast of dark and light regions is from the thickness contrast. The corresponding representative selected area diffraction (SAD) patterns collected from a circular area with a diameter of ~110 nm are demonstrated in (b2) and (c2), respectively. (For interpretation of the references to colour in this figure legend, the reader is referred to the Web version of this article.)

bulk and surface layer, and the thickness measurement of concentrated layers are labeled in Fig. 10c and f, and details are summarized in Table 2. The information is from at least three line scans at different locations to ensure the consistency of measurement. The complete EDS results of the two rings are provided in the Supplementary material. Therefore, when comparing Ring 1 and Ring 6, the increase in cutting speed results in a crystallization of amorphous NiP, along with a P-depleted layer of 15.9 nm. The thickness of the depleted layer by EDS is close to the crystallized layer of 14.2 nm.

Overall, the surface morphology analysis and materials characterization in this study indicate that to achieve high surface quality, the cutting speed should be below a threshold value that induces crystallization in chips and near-surface damage of amorphous NiP.

4. Conclusions

The influence of cutting speed on the surface topography and materials removal mechanisms on fully amorphous NiP was examined by diamond turning with cutting speeds varying from 0.12 m/s to 6.81 m/s. The continuous chipping indicates a continuous ductile machining mode for all cutting speeds. The surface morphology analysis and materials characterization in this study indicate that to achieve high surface quality, the cutting speed should be below a threshold value that induces crystallization in chips and near-surface damage of amorphous NiP. The major observations are as follows.

(a) Surface topography analysis shows that the increase in cutting speed induces higher surface roughness (*Sq*, root mean square roughness) and higher slope of the profile (*Sdq*, root mean square slope). The Pearson correlation coefficient shows that the bias of the roughness shape (*Ssk*, skewness) does not depend on cutting speed but is inversely related to the diameter of the cutting location on the sample disc.
(b) Transmission electron microscopy shows that crystallization is commonly seen in chips for cutting speeds from 0.12 m/s to 6.81 m/s in this study. The portion of crystallized regions is significant, accounting for 25% - 33% based on two long chips in this study.
(c) When comparing the near-surface microstructure in Ring 1 (0.12 m/s) and Ring 6 (6.81 m/s), the increase in cutting speed results in the crystallization of amorphous NiP and a P-depleted layer of 15.9 nm at the surface. The thickness of the depleted layer by EDS is close to that of the crystallized layer of 14.2 nm.

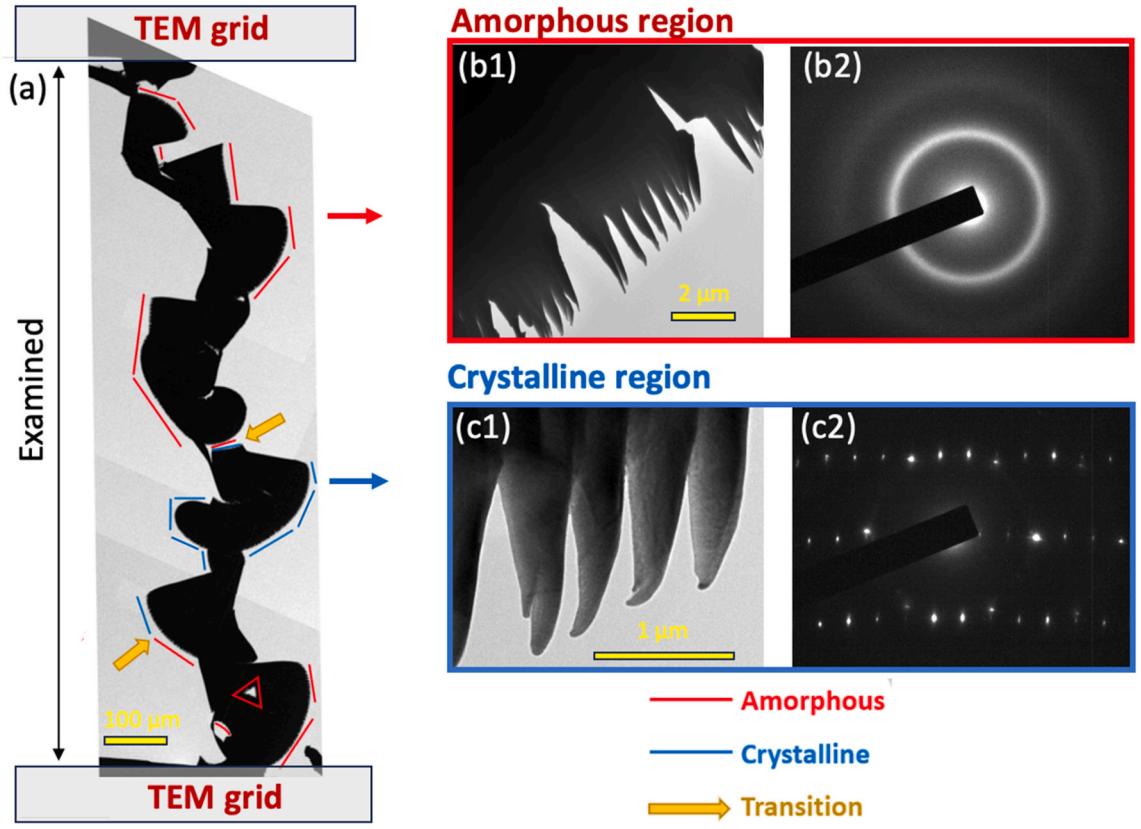

Fig. 7. TEM and SAD analysis of the thinner edges of the entire chip from the highest cutting speed (Ring 6). Similar to Fig. 6, two types of structure: crystalline (red) and amorphous (blue) regions are observed. Amorphous region at high magnification (b1) and corresponding SAD (b2), and crystalline regions at high magnification (c1) and corresponding SAD (c2) are provided. (For interpretation of the references to colour in this figure legend, the reader is referred to the Web version of this article.)

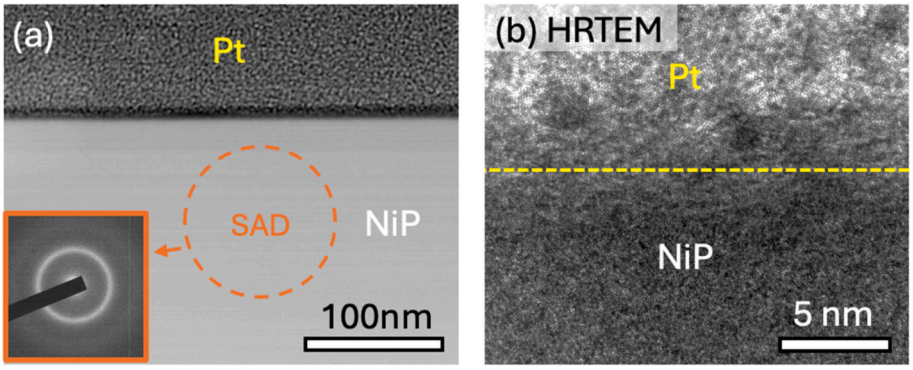

Fig. 8. TEM micrographs of the machined surface region at the lowest cutting speed (Ring 1). (a) The machined surface is protected by Pt, and the inset SAD indicates a clear amorphous structure of NiP. (b) HRTEM micrograph further confirms the structure of the Pt protective layer and NiP; no crystallized layer was detected.

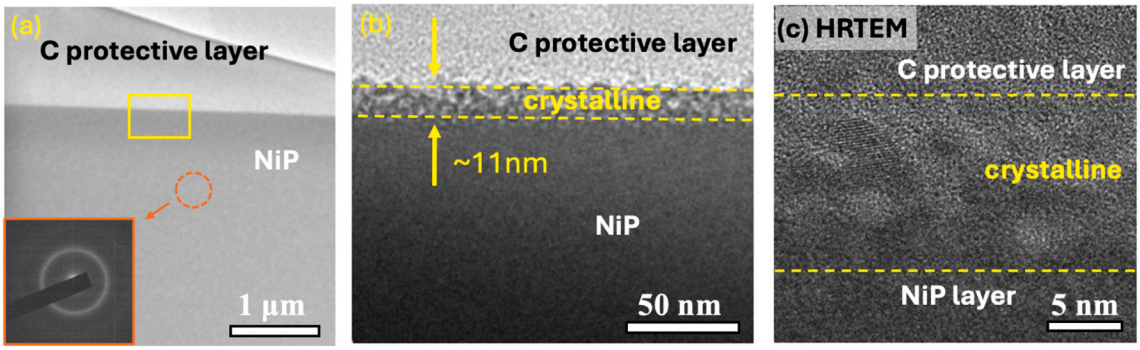

Fig. 9. TEM micrographs of the machined surface region at the highest cutting speed (Ring 6). (a) The machined surface is protected by C, and NiP shows an amorphous structure. (b) A layer of 14.2 nm ± 1.6 nm crystalline structure is observed. (c) HRTEM provides further information that a crystalized layer is formed.

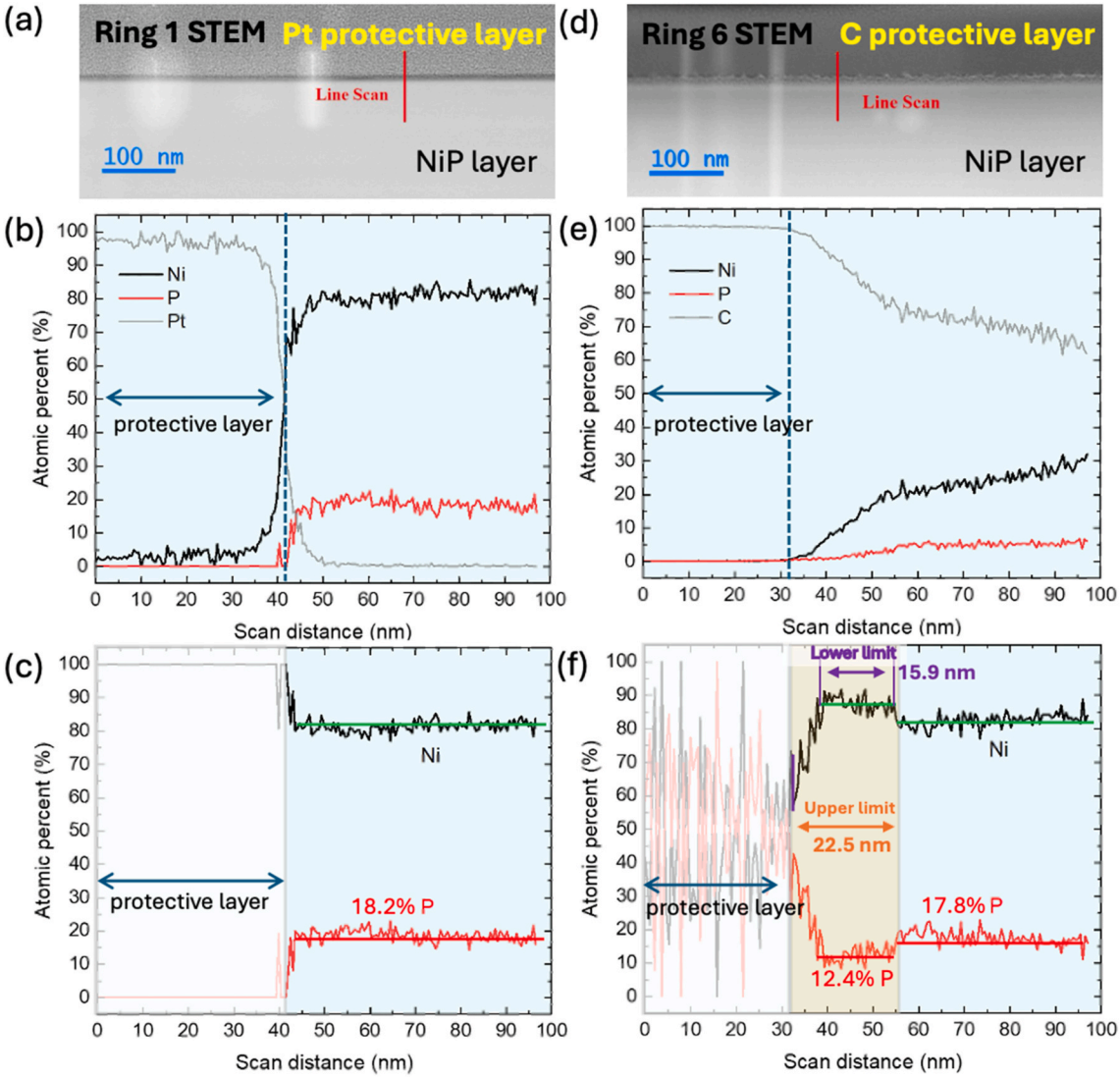

Fig. 10. Elemental investigation of the machined surface region for (a-c) Ring 1 and (d-f) Ring 6 (a,d) STEM images showing the cross-section region of NiP layers protected by Pt or C layers. Representative EDS line scan regions are labeled; (b,e) EDS line scans show the elements of interest, Ni and P, as well as protective layer element (Pt or C); (c,f) Only Ni and P elements are considered for atomic concentration. Protective layers are labeled.

Table 2
Statistical information of P elemental concentrations in the bulk and surface layer of the machined surface, and the thickness measurement of P-depleted layers in the machined surface of Ring 6. The definition of the lower and upper limit is shown in Fig. 10f.

Sample	Bulk concentration	Surface layer concentration	Concentrated thickness (nm)	
	(atomic % P)	(atomic % P)	Lower limit	Upper limit
Ring 1	18.2 ± 0.9	N/A	N/A	N/A
Ring 6	17.8 ± 3.0	12.4 ± 0.6	15.9 ± 0.3	22.5 ± 0.4

CRediT authorship contribution statement

L. Yang: Writing – original draft, Visualization, Investigation. **J. Redford:** Writing – review & editing, Visualization, Methodology, Formal analysis. **T. Liu:** Methodology, Formal analysis. **B. Dutterer:** Methodology, Data curation. **G. Caskey:** Methodology, Formal analysis. **N. Li:** Validation, Methodology, Conceptualization. **C. Evans:** Writing – review & editing, Visualization, Methodology, Funding acquisition, Formal analysis, Conceptualization. **Y. Chen:** Writing – review & editing, Validation, Supervision, Methodology, Investigation, Funding acquisition, Conceptualization.

Declaration of competing interest

The authors declare the following financial interests/personal relationships which may be considered as potential competing interests: Youxing Chen reports financial support was provided by UNC Charlotte. If there are other authors, they declare that they have no known competing financial interests or personal relationships that could have appeared to influence the work reported in this paper.

Acknowledgments

L.Y., C.E. and Y.C. acknowledge financial support by NSF-CMMI 1728554. We are grateful for the useful discussion with Prof. Brigid A. Mullany at UNC Charlotte.

Appendix A. Supplementary data

Supplementary data to this article can be found online at https://doi.org/10.1016/j.precisioneng.2026.03.026.

Data availability

Data used in this study can be supplied by the authors upon reasonable request.

References

[1] Mallory GO, Hajdu JB. Electroless plating: fundamentals and applications, William Andrew. 1990.
[2] Johnson CE. Black electroless nickel surface morphologies with extremely high light absorption capacity. Met Finish 1980;78(7):21–4.
[3] Evans CJ, Polvani RS, Mayer A. Diamond turned electro-deposited nickel alloys, science of optical finishing. Optica Publishing Group; 1990JTuC4.
[4] Paul E, Evans CJ, Mangamelli A, McGlauflin ML, Polvani RS. Chemical aspects of tool wear in single point diamond turning. Precis Eng 1996;18(1):4–19.
[5] Balaraju J, Narayanan TS, Seshadri S. Structure and phase transformation behaviour of electroless Ni–P composite coatings. Mater Res Bull 2006;41(4):847–60.
[6] Wojewoda-Budka J, Wierzbicka-Miernik A, Litynska-Dobrzynska L, Szczerba M, Mordarski G, Mosiałek M, Huber Z, Zieba P. Microstructure characteristics and phase transformations of the Ni-P and Ni-P-Re electroless deposited coatings after heat treatment. Electrochim Acta 2016;209:183–91.
[7] Keong K, Sha W, Malinov S. Crystallisation kinetics and phase transformation behaviour of electroless nickel–phosphorus deposits with high phosphorus content. J Alloys Compd 2002;334(1-2):192–9.
[8] Casstevens JM, Daugherty C. Diamond turning optical surfaces on electroless nickel, precision machining of optics, SPIE. 1978. p. 109–13.
[9] Evans C. Precision engineering: an evolutionary view, Bedford. Cranfield Press; 1989.
[10] Rhorer RL, Evans CJ. Fabrication of optics by diamond turning, chapter 41, handbook of optics. 2010.
[11] S.R. Patterson, Private communication: regarding the "beauty is in the details" Philosophy in precision engineering., in: C. Evans (Ed.).
[12] Field JE. The properties of natural and synthetic diamond. 1992.
[13] Kawasegi N, Ozaki K, Morita N, Nishimura K, Sasaoka H. Single-crystal diamond tools formed using a focused ion beam: tool life enhancement via heat treatment. Diam Relat Mater 2014;49:14–8.
[14] Taylor JS, Syn CK, Saito TT, Donaldson RR. Surface finish measurements of diamond-turned electroless-nickel-plated mirrors. Opt Eng 1986;25(9):1013–20.
[15] Crompton D, Hirst W, Howse M. The wear of diamond. Proceed Royal Soc London A Math Phys Sci 1973;333(1595):435–54.
[16] Dini J, Donaldson R, Syn C, Sugg D. Diamond tool wear of electrodeposited nickel-phosphorus alloy. CA (USA): Lawrence Livermore National Lab.; 1990.
[17] Gebhardt A, Kinast J, Rohloff R-R, Seifert W, Beier M, Scheiding S, Peschel T. Athermal metal optics made of nickel plated AlSi40. International Conference on Space Optics—ICSO 2014, SPIE. 2017. p. 451–9.
[18] Goldman A, Long G, Bennett L, Lashmore D, Kuriyama M. Observation of two structurally distinct states in Ni-P glasses using EXAFS. J Electrochem Soc 1988;135(8):1919.
[19] Lashmore D, Bennett L, Schone H, Gustafson P, Watson R. Polymorphism of nickel-phosphorus metallic glasses. Phys Rev Lett 1982;48(25):1760.
[20] Dogra M, Sharma V, Dureja J. Effect of tool geometry variation on finish turning-A review. J Eng Sci Technol Rev 2011;4(1).
[21] Cheung CF, Lee WB. A theoretical and experimental investigation of surface roughness formation in ultra-precision diamond turning. Int J Mach Tool Manufact 2000;40(7):979–1002.
[22] Geng R, Yang X, Xie Q, Zhang W, Kang J, Liang Y, Li R. Ultra-precision diamond turning of ZnSe ceramics: surface integrity and ductile regime machining mechanism. Infrared Phys Technol 2021;115:103706.
[23] Ruibin X, Wu H. Study on cutting mechanism of Ti6Al4V in ultra-precision machining. Int J Adv Manuf Technol 2016;86(5):1311–7.
[24] Zhang C-M, Mu A-L, Wang Y-X, Wang Y, Zhang Y. Influence of turning parameters on turning performance of ultra-high strength steel. Integrated Ferroelectrics Int J 2020;209(1):110–8.
[25] Kim WK, Kim GH, Ryu GM. A study on the characteristics for ultra-precision machining technique using single diamond turning machine. SPIE: Optical Manufacturing and Testing X; 2013. p. 296–303.
[26] Bao X, Yao P, Xu J, Mei Z, Li Y, Yang J, Wang Q, Chen Z, Qu S, Huang C. Effect of tool geometry and cutting parameters on surface quality and chip morphology of amorphous electroless nickel-phosphorus alloy in ultra-precision turning. Int J Adv Manuf Technol 2023;126(5):2461–78.
[27] Yan J, Asami T, Harada H, Kuriyagawa T. Crystallographic effect on subsurface damage formation in silicon microcutting. CIRP Ann 2012;61(1):131–4.
[28] Chen J, Ding F, Luo X, Rao X, Sun J. Fundamental study of ductile-regime diamond turning of single crystal gallium arsenide. Precis Eng 2020;62:71–82.
[29] Astakhov VP. Turning, modern machining technology. 2011. p. 1–78. Elsevier.
[30] ISO 25178-2:2021 geometrical product specifications (gps) — surface texture: areal — part 2: terms, definitions and surface texture parameters. .